EINDHOVEN UNIVERSITY OF TECHNOLOGY

Low resistivity HfN_x grown by plasma-assisted ALD with external rf substrate biasing

Citation for published version (APA):
Karwal, S., Verheijen, M. A., Williams, B. L., Faraz, T., Kessels, W. M. M., & Creatore, M. (2018). Low resistivity HfN_x grown by plasma-assisted ALD with external rf substrate biasing. *Journal of Materials Chemistry C*, *6*(15), 3917-3926. https://doi.org/10.1039/C7TC05961B

Document license:
TAVERNE

DOI:
10.1039/C7TC05961B

Document status and date:
Published: 21/04/2018

Document Version:
Publisher's PDF, also known as Version of Record (includes final page, issue and volume numbers)

Please check the document version of this publication:

• A submitted manuscript is the version of the article upon submission and before peer-review. There can be important differences between the submitted version and the official published version of record. People interested in the research are advised to contact the author for the final version of the publication, or visit the DOI to the publisher's website.
• The final author version and the galley proof are versions of the publication after peer review.
• The final published version features the final layout of the paper including the volume, issue and page numbers.

Link to publication

General rights
Copyright and moral rights for the publications made accessible in the public portal are retained by the authors and/or other copyright owners and it is a condition of accessing publications that users recognise and abide by the legal requirements associated with these rights.

• Users may download and print one copy of any publication from the public portal for the purpose of private study or research.
• You may not further distribute the material or use it for any profit-making activity or commercial gain
• You may freely distribute the URL identifying the publication in the public portal.

If the publication is distributed under the terms of Article 25fa of the Dutch Copyright Act, indicated by the "Taverne" license above, please follow below link for the End User Agreement:

www.tue.nl/taverne

Take down policy
If you believe that this document breaches copyright please contact us at:

openaccess@tue.nl

providing details and we will investigate your claim.

Download date: 28. Mar. 2025

Journal of Materials Chemistry C

ROYAL SOCIETY OF CHEMISTRY

PAPER

View Article Online
View Journal

Published on 12 March 2018. Downloaded by Eindhoven University of Technology on 28/03/2018 21:38:44.

Cite this: DOI: 10.1039/c7tc05961b

Low resistivity HfN_x grown by plasma-assisted ALD with external rf substrate biasing†

S. Karwal,[a] M. A. Verheijen,[ab] B. L. Williams,[a] T. Faraz,[a] W. M. M. Kessels[ac] and M. Creatore*[ac]

Plasma-assisted atomic layer deposition (ALD) of HfN_x thin films using tris(dimethylamino)cyclopentadienylhafnium [$CpHf(NMe_2)_3$] as the Hf precursor and H_2 plasma as the reducing co-reactant is reported. We previously concluded that the HfN_x films prepared for a grounded substrate (0 V substrate potential) exhibited a rather high electrical resistivity of 9.0×10^{-1} Ω cm. In the present work, we show a steady decrease in the electrical resistivity by two orders of magnitude to 3.3×10^{-3} Ω cm upon increasing the time-averaged substrate potential up to −130 V by externally biasing the substrate. A further increase in potential up to −187 V led to an increase in electrical resistivity to 1.0×10^{-2} Ω cm. The variations in electrical resistivity with the potential were found to correlate with the extent of grain boundary scattering in the films, which significantly decreased upon increasing the potential up to −130 V, primarily due to major changes in the film chemical composition. The latter consisted in a decrease in O content from 20.1 at% under no bias to ≤ 2 at% for a potential of −130 V and an associated increase in the Hf^{3+} fraction from 0.65 to 0.82. The latter is key to the development of low resistivity δ-HfN. A further increase in potential to −187 V led to an increase in grain boundary scattering as a consequence of a major decrease in grain size as well as in-grain crystallinity. In view of advanced nanoelectronic devices, the HfN_x layers were also deposited on 3D trench nanostructures at a potential of −130 V. A low oxygen content in the HfN_x film was measured on both the planar and vertical topographies of the trenches. Overall, the time-averaged substrate potential has been shown to highly affect the chemical composition, microstructure and the associated electrical properties of the HfN_x layers and can be used to tailor the HfN_x film properties.

Received 28th December 2017,
Accepted 12th March 2018

DOI: 10.1039/c7tc05961b

rsc.li/materials-c

Introduction

Conductive transition metal nitride (TMN) films are widely employed in microelectronics because of their low electrical resistivity,[1,2] and excellent diffusion barrier properties against oxygen and copper.[3–6] In particular, conductive titanium nitride and tantalum nitride films have been already implemented as gate metals in metal oxide semiconductor field-effect transistors (MOSFETs). One of the issues encountered in their implementation is the formation of oxy-nitrides at the interface with the gate oxide.[1,7,8]

[a] *Department of Applied Physics, University of Technology Eindhoven, 5600MB, P.O. Box 513, Eindhoven, The Netherlands. E-mail: m.creatore@tue.nl*
[b] *Philips Innovation Labs, High Tech Campus 11, 5656 AE Eindhoven, The Netherlands*
[c] *Solliance, High Tech Campus 21, 5656AE, Eindhoven, The Netherlands*

† Electronic supplementary information (ESI) available: ALD recipe schematic and saturation details, deconvolution of imaginary dielectric function (ε_2) into various oscillators and Drude absorption for HfN_x films, XPS O 1s and C 1s deconvolutions, table with XPS spectral lines, variation of GPC (Å) with GPC (Hf atoms nm^{-2}) and HAADF-STEM images and SAED patterns of HfN_x nucleation layer. See DOI: 10.1039/c7tc05961b

In photovoltaics, they are of interest due to the extended high near-IR reflectivity.[9,10] Zirconium nitride has been employed as a back reflector electrode for thin-film copper–indium–gallium–selenide (CIGS) solar cells.[11] Recently, low resistivity hafnium nitride films (δ-HfN) have gained notable importance because of their superior stability when used in combination with HfO_2.[6] Furthermore, a very-high reflectivity in the spectral region between 1 eV and 2.4 eV,[2] allows applications such as back reflectors for CIGS solar cells and as heat mirrors.[12,13]

Hafnium nitride (HfN_x) exists in different crystal phases including highly resistive Hf_3N_4,[14,15] and the conductive δ-HfN fcc phase.[9,16] Therefore, it can be inferred that the oxidation state of Hf in the film (Hf^{4+} *vs.* Hf^{3+}) and the stoichiometry fundamentally affect the HfN_x material properties. Thin films of δ-HfN_x have been grown by various methods, such as physical vapour deposition (PVD),[10,17,18] metal–organic chemical vapour deposition (MO-CVD)[19] and atomic layer deposition (ALD).[20–22] Due to the stringent requirements posed by the semiconductor industry as a result of device shrinkage, especially ALD has emerged as a key deposition technique which holds the promise of delivering ultra-thin films with precise thickness control,

Published on 12 March 2018. Downloaded by Eindhoven University of Technology on 28/03/2018 21:38:44.

excellent uniformity, and unparalleled conformality on high surface area substrates.[23–26]

With regard to the δ-HfN material properties, Seo *et al.* obtained a very low electrical resistivity (ρ_e) of 1.4×10^{-5} Ω cm for a 650 nm thick single crystal δ-HfN film grown by PVD.[18] On the other hand, the preparation of low resistivity δ-HfN_x films by either CVD or ALD employing metal–organic Hf precursors and a reducing co-reactant, is challenging. This is primarily due to the incomplete abstraction of ligands leading to impurities in the film and/or inefficient reduction of the Hf^{4+} oxidation state (in the precursor) to Hf^{3+} (in the film). Kim *et al.* reported the MO-CVD growth of the δ-HfN film with an ρ_e of 1.0×10^{-3} Ω cm for a ∼1 μm thick film using an alkylamide Hf precursor and *N*,*N*-dimethylhydrazine as the reducing agent. In contrast, non-conducting Hf_3N_4 films were obtained when NH_3 was used as the reducing agent.[19] This illustrates that the potential for the reduction of M^{4+} to M^{3+} (M = metal atom) dictates the choice in reducing the co-reactant, which as such, can significantly alter the film properties.[22]

The growth of ultra-thin δ-HfN_x films by ALD has been reported by Consiglio *et al.* and Kim *et al.* by employing a highly reducing H_2 plasma as co-reactant and using alkylamide Hf precursors.[20,21] Consiglio *et al.* reported an ρ_e of 2.3×10^{-3} Ω cm (film thickness is not reported),[20] whereas Kim *et al.* obtained an ρ_e of 6.7×10^{-3} Ω cm for a film thickness of 14 nm.[21] For these films, the fraction of the Hf^{3+} oxidation state in the layers was not reported. Moreover, besides the chemical composition, it can be expected that also the microstructure of the layer is crucial for HfN_x film resistivity. This effect has been only sparsely investigated so far.

Recently, we have shown the importance of selecting the composition of the plasma gas as a co-reactant to control the chemical composition and microstructure of HfN_x thin films.[22] We demonstrated the necessity of a reducing H_2 plasma in order to fabricate the conductive δ-HfN_x phase.[22] However, the HfN_x films grown using H_2 plasma resulted in relatively high ρ_e values of $(9.0 \pm 0.2) \times 10^{-1}$ Ω cm.[22] We observed that the film contained 20.1 ± 0.7 O at% leading to the formation of Hf–O bonds and resistive films. In a conductive δ-HfN phase, the Hf exists in the 3+ oxidation state with loosely bound 5d electrons serving as free carriers.[10] The presence of Hf–O bonds increased the oxidation state of Hf to 4+, which limited the Hf^{3+} oxidation state fraction down to 0.65 ± 0.02 for the aforementioned H_2 plasma case. This decreased the conduction electron density and increased the film resistivity.[22]

Building on earlier studies, the seminal work of Anders showed that the mean energy of ion bombardment can play a central role in determining the film properties in the case of PVD.[27] Furthermore, selected effects of energetic ion bombardment on the film properties during a PE-CVD processes have been reported.[28,29] Regarding plasma-assisted ALD processes, Profijt *et al.* introduced the aspect of increasing the ion energy by externally biasing the substrate with an rf power source and studied the resulting ion energy distributions.[30] In this case, the bias was applied only during the plasma half cycle and it was found to tune the crystalline phase of TiO_2 films as well as increase the mass density of Co_3O_4 films.[30]

In this work, we will address the impact of an external rf substrate bias during the H_2 plasma half cycle on the HfN_x films prepared by ALD. The time-averaged substrate potential (V_{bias}, developed upon application of external rf substrate bias) is shown to highly affect the material properties of HfN_x films. We observed a steady decrease in the ρ_e of the HfN_x films to a minimum of $(3.3 \pm 0.1) \times 10^{-3}$ Ω cm upon increasing the $|V_{bias}|$ up to 130 V. In contrast, we observed an increase in the ρ_e to $(1.0 \pm 0.3) \times 10^{-2}$ Ω cm upon further increasing the $|V_{bias}|$ from 130 V to 187 V. We found that the variations in the ρ_e with $|V_{bias}|$ correlates with the extent of grain boundary scattering in the films, which significantly decreased upon increasing the $|V_{bias}|$ up to 130 V. The decrease in ρ_e and scattering is due to a substantial decrease in O content (down to ≤2 at%) and an associated improvement in the Hf^{3+} fraction to 0.82 ± 0.02 since the HfN_x films grown at $|V_{bias}|$ = 130 V are found to be considerably more porous than the HfN_x films prepared with a grounded electrode. A further increase in the $|V_{bias}|$ to 187 V led to a major decrease in grain size as well as in-grain crystallinity, culminating in an increase in scattering and ρ_e of the films. The HfN_x was also deposited on 3D trench nanostructures to investigate the chemical composition at different regions (planar and vertical sidewalls), as is relevant for advanced nanoscale device architectures. The HfN_x layer grown at $|V_{bias}|$ = 130 V showed a reduced O content on both the planar and vertical regions of the trench structures. The low O content on the vertical regions suggests that the ion bombardment reaches also the sidewalls, most certainly due to collisions between ions in the plasma sheath with background gas. The obtained results elucidate the importance of ions and their energy in improving the chemical composition/microstructure and the associated electrical properties of HfN_x layers.

Experimental section

Plasma-assisted ALD of HfN_x and process conditions.

HfN_x thin films were deposited using an Oxford Instruments FlexAL ALD reactor,[31,32] equipped with an inductively coupled remote plasma (ICP) source with an alumina dielectric tube. A base pressure of 1.6×10^{-6} Torr was achieved in the reactor chamber using a turbo-molecular pump before every deposition. A stage temperature of 450 °C was selected for HfN_x ALD (corresponding to a substrate temperature of 340 °C as estimated from spectroscopic ellipsometry (SE)), since the onset of precursor decomposition and ingress of the CVD regime was observed above 450 °C (see ESI,† Fig. S2c).[22] The reactor walls were kept at 145 °C during all the depositions.

A stainless steel bubbler contained the Hf precursor $CpHf(NMe_2)_3$ (Air Liquide, >99.99% purity) at 60 °C and was bubbled by an Ar flow of 100 sccm. An Ar flow of 100 sccm was injected into the ICP alumina tube during the precursor dosage in order to suppress deposition on the ICP tube walls (the gate valve between the ICP source and reactor chamber was kept open during the full cycle). During the plasma exposure, H_2 (>99.999% purity, working pressure ∼30 mTorr) at 100 sccm was introduced into the chamber and subsequently the plasma

 This journal is © The Royal Society of Chemistry 2018

Published on 12 March 2018. Downloaded by Eindhoven University of Technology on 28/03/2018 21:38:44.

was ignited with 100 W radio frequency (rf) ICP power (13.56 MHz) for the desired time (see Fig. S1, ESI† for ALD recipe). The purge step for both half cycles consisted of a flow of 200 sccm Ar through the bubbling lines and 100 sccm Ar flow from the ICP source with the valve to the pump fully opened. As reported previously, a $CpHf(NMe_2)_3$ pulse length of 4 s and a H_2 plasma exposure of 10 s was used, while keeping the purge step of 2 s after every half cycle (Fig. S2, ESI†).[22]

RF substrate biasing

Employing the special feature of the latest Oxford Instruments FlexAL systems, an external substrate bias was applied during the H_2 plasma exposure using a rf power source (13.56 MHz), attached to the substrate table (Fig. S1, ESI†). The magnitude of the developed time-averaged substrate potential with respect to ground is indicated by V_{bias}. During the H_2 plasma exposure, this value was regulated by varying the applied rf power. Shown in Fig. 1a are the rf bias voltage waveforms as a function of time. These are measured using an oscilloscope connected to the substrate table *via* a high voltage probe. Fig. 1a also shows that a time-averaged negative potential with respect to ground (V_{bias}) has developed at the substrate such that the flux of electrons equals the flux of ions, when integrated over one period of the rf waveform.[30] The amplitude of the voltage and V_{bias} can be regulated by varying the power applied to the substrate table. A V_{bias} = −80 V is obtained when 10 W rf bias power is applied, whereas V_{bias} = −187 V results from 40 W rf power. The plot of the absolute values of V_{bias} as a function of rf bias power (Fig. 1b) shows a deviation from the ideal linear behaviour.

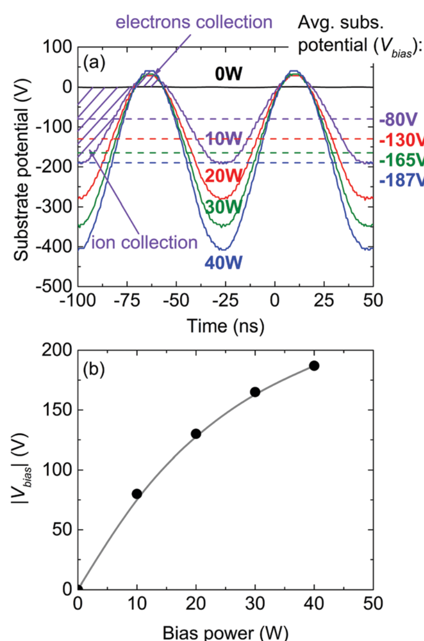

Fig. 1 (a) Substrate potential waveforms as a function of time measured using an oscilloscope: the development of time-averaged substrate potential V_{bias} with respect to ground can be observed (b) absolute values of V_{bias} as a function of the applied rf bias power. The line serves as a guide to the eye.

This deviation may be due to heating of the electrons near the substrate generating an additional plasma which increases the ion current, as well as to other effects such as power dissipation by resistive losses at the substrate or in the matching network.

As a result of the voltage drop over the plasma sheath, the ions are accelerated towards the surface. For a collisionless sheath, the corresponding average ion energy (E_{ion}) is given by $E_{ion} = e(V_p - V_{bias})$, where V_p is the plasma potential.[30] Profijt *et al.* showed that the E_{ion} is 20–30 eV for a grounded electrode (no external substrate bias) using H_2 plasma in a similar FlexAL system and under similar experimental conditions.[33] This implies that the E_{ion} under rf substrate biasing conditions is expected to be approximately 20–30 eV higher than the value of $e|V_{bias}|$. We note however that the actual ion energy distribution function is bimodal,[30] and that the plasma sheath is not fully collisionless as will be addressed in future work.

Substrates and material characterization

The HfN_x films were deposited on Si(100) substrates with a diameter of 100 mm and with 450 nm SiO_2 atop. The growth per cycle (GPC) and the dielectric functions of the HfN_x films were examined *via* spectroscopic ellipsometry (SE) (J.A. Woollam, Inc., M2000U). The dielectric functions ($0.75 \le h\nu \le 5.0$ eV) of HfN_x films were modelled using one Drude and two Lorentz oscillators as demonstrated by Hu *et al.* (see Fig. S4a and Table S1, ESI† for details).[9] Additionally, the optical resistivity (ρ_{op}) (at room temperature) was deduced from the free-carrier Drude parameterization, given by

$$\rho_{op} = \Gamma_D/\varepsilon_o \cdot \omega_p^2,$$

where Γ_D is the damping factor for the Drude oscillator, ε_o is the permittivity of free space, and ω_p is the screened plasma frequency.[34] The electrical resistivity (ρ_e) (at room temperature) was obtained *via* four-point probe measurements using a Keithley 2400 SourceMeter and a Signaton probe by multiplying the sheet resistance of the HfN_x films with the film thickness as derived from SE.

The X-ray photoelectron spectroscopy (XPS) measurements were performed using a Thermoscientific K-Alpha KA1066 system equipped with a monochromatic Al Kα ($h\nu$ = 1486.6 eV) source in order to study the chemical bonding and the oxidation states of elements present in the film. The chemical composition and the mass density of the films was evaluated *via* Rutherford backscattering spectrometry (RBS) and elastic recoil detection (ERD) using 1900 keV $^4He^+$ ions (Detect99). For the ERD measurements, the recoil angle was 30° and the angle of incidence with the sample surface was kept at 15° whereas for the RBS, two detectors were used with scattering angles of 170° and 150°.

The HfN_x film microstructure was studied using transmission electron microscopy (TEM) using a JEOL ARM 200F, operated at 200 kV. Selected area electron diffraction (SAED) patterns of 1.3 μm diameter area were acquired from ∼15 nm thick HfN_x films, grown at various values of V_{bias} in order to study the texture evolution and lateral crystallite sizes during the film nucleation. The HfN_x films were grown on SiN_x TEM windows, coated with ∼5 nm ALD SiO_2.

Published on 12 March 2018. Downloaded by Eindhoven University of Technology on 28/03/2018 21:38:44.

The crystallinity of the films was examined with a PANalytical X'pert PRO MRD X-ray diffractometer using a Cu Kα (λ = 1.542 Å) X-ray source. The X-ray diffractograms were obtained for $\sim$75 nm thick HfN_x films in a θ–2θ configuration and were compared with the powder HfN and Hf_2ON_2 patterns.[35,36] The vertical crystallite sizes were computed using the X-ray line broadening in the Scherrer's equation. The broadening of the peak in XRD primarily arises from the presence of stress and/or crystallite size.[37] For the computation of the crystallite size in our case, the film stress was neglected.

The surface morphology and lateral grain size for $\sim$75 nm thick HfN_x films was studied using a Zeiss Sigma field emission scanning electron microscope (FE-SEM) operated at an acceleration voltage of 2 kV.

The residual film stress was calculated using a Tencor FLX-2320 by evaluating the laser deflection as a result of change in the curvature of the Si wafer using Stoney's equation.[38]

The HfN_x films were also deposited on trench nanostructures with a varying aspect ratio (height $\sim$450 nm, width varying) in order to evaluate the chemical composition on 3D topographies. Coupons containing these trench nanostructures were prepared and provided by LAM Research.[39] The respective 3D trench nanostructures were formed by first depositing thick the SiO_2 film on Si wafer *via* PECVD, which was then etched into trench structures. These structures were subsequently coated with a conformal SiN_x layer using a high-temperature CVD process, followed by deposition of a very thin layer of SiO_2 using ALD.[39] Following the HfN_x ALD, a thin lamella ($\sim$100 nm) was prepared by a focused ion beam (FIB) using the lift-out preparation procedure. Scanning TEM combined with energy-dispersive X-ray spectroscopy (EDX) was used to study the chemical composition of the deposited HfN_x films.

Results and discussions

We previously reported on HfN_x films ($\sim$70 nm thick) prepared with a grounded electrode ($|V_{bias}|$ = 0 V), reaching an ρ_e of $(9.0 \pm 0.2) \times 10^{-1}$ Ω cm.[22] In addition, the opto-electronic properties of the HfN_x films were probed using SE. Fig. S4b (ESI†) shows the imaginary part of the dielectric function ε_2 and the corresponding Drude absorption for the HfN_x films prepared at various values of $|V_{bias}|$. Using the magnitude of the Drude absorption, we previously reported an optical resistivity (ρ_{op}) of $(5.9 \pm 0.1) \times 10^{-3}$ Ω cm for the HfN_x films prepared at $|V_{bias}|$ = 0 V.[22]

The effect of an external rf substrate bias on the HfN_x material properties was evaluated. For these experiments, only $|V_{bias}|$ was varied during the H_2 plasma half cycle, whereas the $CpHf(NMe_2)_3$ pulse length of 4 s and H_2 plasma exposure of 10 s was kept constant.[22] A comprehensive summary of several material properties of HfN_x films prepared on planar SiO_2/Si substrates for various values of $|V_{bias}|$ (constant film thickness $\sim$70–80 nm) can be found in Table 1.

The variations in the electrical and opto-electronic properties of the HfN_x films with $|V_{bias}|$ are discussed at first. Fig. 2a shows

Table 1 The properties of HfN_x films prepared at various values of $|V_{bias}|$, as determined by a four-point probe (FPP), spectroscopic ellipsometry (SE), X-ray photoelectron spectroscopy (XPS), Rutherford backscattering (RBS) and elastic recoil detection (ERD). The electrical resistivity was obtained by a combination of FPP and SE whereas the optical resistivity, GPC and thickness were determined using SE. XPS was used to obtain the Hf^{3+} oxidation state fraction and the chemical composition and the GPC values in terms of number of deposited Hf at nm^{-2} $cycle^{-1}$ were determined by RBS. The H content was determined using ERD. The mass density was calculated by dividing the areal mass density (obtained *via* RBS and ERD) with the film thickness. The errors for the electrical resistivities and optical resistivities are less than 3% and 2% of their absolute values, respectively. The errors for the GPC, the Hf^{3+} fraction and the mass densities are mentioned in the first line unless otherwise mentioned

	FPP	SE			XPS	RBS					ERD
$\lvert V_{bias}\rvert$ (V)	Electrical resistivity (Ω cm)	Optical resistivity (Ω cm)	GPC (Å)	Thickness (nm)	Hf^{3+}/(Hf^{3+} + Hf^{4+})	GPC (Hf at nm^{-2} $cycle^{-1}$)	N/Hf	C (at%)	O (at%)	Mass density (g cm^{-3})	H (at%)
0	9.0×10^{-1}	5.9×10^{-3}	0.35 ± 0.03	71	0.65 ± 0.02	0.82 ± 0.04	0.86 ± 0.05	<2.0	20.1 ± 0.7	8.2 ± 0.2	7.0 ± 0.3
130	3.3×10^{-3}	9.0×10^{-4}	0.50	81	0.82	1.53 ± 0.06	1.00 ± 0.07	11.0 ± 1.2	<2.0	8.6	12.6 ± 0.6
187	1.0×10^{-2}	1.7×10^{-3}	0.60	83	0.73	1.76 ± 0.06	0.98 ± 0.06	10.3 ± 1.1	<2.0	8.0	18.5 ± 0.9

This journal is © The Royal Society of Chemistry 2018

Published on 12 March 2018. Downloaded by Eindhoven University of Technology on 28/03/2018 21:38:44.

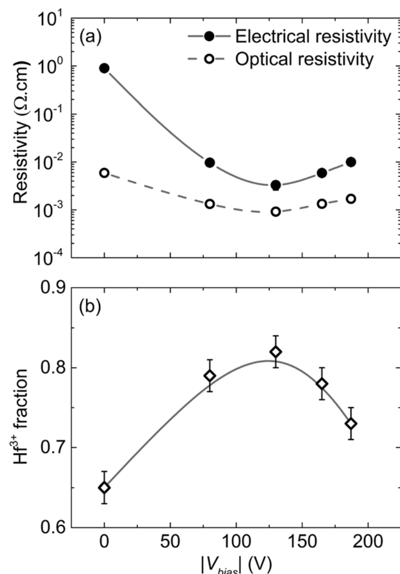

Fig. 2 (a) Electrical and optical resistivity values and (b) Hf^{3+} oxidation state fraction of HfN_x films as a function of the absolute value of V_{bias}. Lines serve as a guide to the eye.

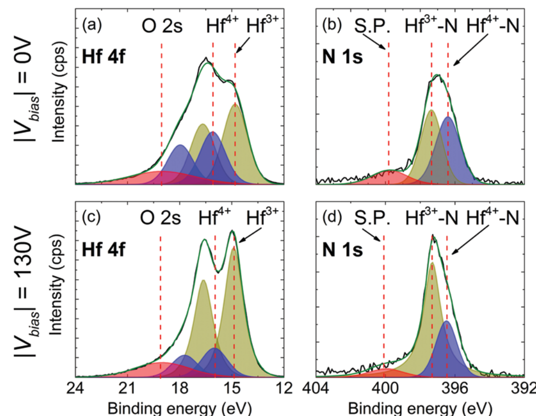

Fig. 3 Deconvoluted XPS spectra for HfN_x films prepared at $|V_{bias}|$ = 0 V and $|V_{bias}|$ = 130 V for Hf 4f with Hf^{3+} and Hf^{4+} oxidation states (a and c), and N 1s with associated bonding to Hf atoms (c and d). Data for $|V_{bias}|$ = 0 V is given in (a) and (b) and data for $|V_{bias}|$ = 130 V is given in (c) and (d) S.P. represents the satellite peak.

the ρ_e and ρ_{op} for HfN_x films as a function of $|V_{bias}|$. Remarkably, the ρ_e decreased by two orders to a value of $(3.3 \pm 0.1) \times 10^{-3}$ Ω cm at $|V_{bias}|$ = 130 V, as compared to the films prepared with the grounded electrode. In parallel, an increase in the $|V_{bias}|$ to 130 V led to an increase in Drude absorption resulting in a decrease of ρ_{op} to $(9.0 \pm 0.2) \times 10^{-4}$ Ω cm (Fig. S4b, ESI†). On the other hand, a further increase in the $|V_{bias}|$ to 187 V led to a subsequent increase in ρ_e to $(1.0 \pm 0.3) \times 10^{-2}$ Ω cm and ρ_{op} to $(1.7 \pm 0.1) \times 10^{-3}$ Ω cm.

By considering the rather small interaction distance of incident light with the HfN_x films (∼2–3 nm) (see ESI†), the difference between the ρ_e and ρ_{op} may provide insights into the extent of grain boundary scattering phenomena as described by Knoops *et al.*[22,34] The large difference between the ρ_e and ρ_{op} values at $|V_{bias}|$ = 0 V suggests the presence of prominent grain boundary scattering in the HfN_x films. Interestingly, the resistivity difference decreased significantly by the application of external rf substrate bias and attained a minimum at $|V_{bias}|$ = 130 V (Fig. 2a). This indicates a decrease in the scattering at grain boundaries, which reduces the resistance in the transport of the electrons between adjacent grains. On further increasing the $|V_{bias}|$ to 187 V, the resistivity difference increased slightly, indicating an increase in the scattering in the film at high values of V_{bias}. The grain boundary scattering may arise from several factors such as a high barrier height at the grain boundaries and/or a low in-grain electron density.[40] Furthermore, smaller grains may result in larger grain boundary scattering if the grain boundaries are poorly passivated.[34] Therefore, in order to understand the variation in grain boundary scattering and the associated ρ_e with $|V_{bias}|$, the chemical composition and microstructure of the HfN_x films was studied.

The chemical composition of HfN_x films was investigated by means of RBS and XPS. We previously reported that HfN_x films grown at $|V_{bias}|$ = 0 V contained <2.0 at% C and that the 10 s H_2 plasma exposure was sufficiently long for complete abstraction of the carbon groups from the adsorbed precursor (Table 1).[22] Furthermore, the HfN_x film was found to contain 20.1 ± 0.7 at% O.[22] We showed that oxygen was primarily incorporated during deposition and not because of post-deposition oxidation.[22] We also demonstrated that the O present in the films selectively formed Hf–O bonds (see the deconvolution of the O 1s XPS spectrum in Fig. S5a, ESI†),[41] which can be related to the high enthalpy of formation of HfO_2 (−1144.7 kJ mol^{-1}) and HfO (−564.8 kJ mol^{-1})[42] as compared with the enthalpy of formation of HfN (−369 kJ mol^{-1}).[43] This limited the Hf^{3+} oxidation state fraction to a relatively low value of 0.65 ± 0.02 (Fig. 2b, 3a and Table 1).

Interestingly, the Hf^{3+} fraction steadily increased to 0.82 ± 0.02 upon increasing the $|V_{bias}|$ value up to 130 V as shown in Fig. 2b and 3c, in-line with the aforementioned decrease in the ρ_{op}. On the other hand, when $|V_{bias}|$ is increased to 187 V, the Hf^{3+} fraction decreases again to 0.73 ± 0.02, in-line with the increase in the ρ_{op}. The increase in the Hf^{3+} fraction with $|V_{bias}|$ up to 130 V occurs in parallel with the decrease in O content to ≤2.0 at% for the $|V_{bias}|$ value of 130 V or higher. Relevantly, preliminary density functional theory studies suggest that an increase in the energy of bombarding ions may promote desorption of H_2O from the surface of the film, resulting in lower oxygen content upon increasing $|V_{bias}|$. The decrease in the Hf^{3+} fraction upon further increasing the $|V_{bias}|$ to 187 V is speculated to arise from an increase in the H content (Table 1) and the associated Hf–H bonds, as the O content in the HfN_x films grown above $|V_{bias}|$ value of 130 V remains similar. This may lead to an increase in the Hf^{4+} relative content.

Nitrogen was also found to exist in two chemical environments, *i.e.* bonding with Hf^{3+} and Hf^{4+} atoms as presented in Fig. 3b and d (see Table S2 (ESI†) for a summary of the binding energies for different elements).[44,45] The application of an external rf substrate bias ($|V_{bias}|$ = 130 V) increased the number of N atoms bonded to Hf atoms that are present in the 3+ oxidation state, when compared with the grounded electrode condition. This result

Published on 12 March 2018. Downloaded by Eindhoven University of Technology on 28/03/2018 21:38:44.

corroborates the increase in the fraction of the δ-HfN phase. In contrast to the O content, the C concentration increased by the application of an external rf substrate bias (Table 1). Fig. S5b (ESI†) shows the C 1s XPS spectra of the bulk HfN_x films as a function of $|V_{bias}|$. The peak at lower binding energy (282 eV) is attributed to Hf–C bonding.[46] A steady increase in the Hf–C peak intensity is observed upon increasing the $|V_{bias}|$ from 0 V up to 130 V. These results suggest that the carbon in the films may originate from the enhanced cracking of the ligands on the surface by energetic ion bombardment, followed by re-deposition.[32] Alternatively, carbon-containing cationic species in the plasma may also get accelerated towards the growing film (a kind of redeposition) that may also lead to carbon incorporation.

Fig. 4 shows the effect of external rf substrate bias application on the GPC in terms of the thickness (Å) and areal density of deposited Hf atoms (Hf atoms nm^{-2}), whereas an elaborate characterization of the ALD process (linear thickness increase, self-saturation behaviour and thickness uniformity maps for HfN_x films) as a function of $|V_{bias}|$ is shown in the ESI† (Fig. S3). The ALD process was found to saturate for all values of $|V_{bias}|$ investigated. A consistent increase in GPC (Å) with $|V_{bias}|$ was observed, which may result from an increase in precursor adsorption, decrease in film mass density and/or changes in chemical composition. By means of RBS, we found that the areal density of deposited Hf atoms per cycle also increased with $|V_{bias}|$. This indicates that the precursor adsorption increases with $|V_{bias}|$, which may occur due to the presence of a higher density of active sites for precursor adsorption after every ALD cycle. By plotting the GPC (Å) as a function of the areal density of Hf atoms deposited per cycle (Fig. S6, ESI†), we found roughly a linear dependence. Therefore, it can be concluded that the increase in the GPC (Å) with the $|V_{bias}|$ is primarily due to an increase in precursor adsorption. Furthermore, the application of external rf substrate bias resulted in N/Hf ratio of 1.00 ± 0.07 and 0.98 ± 0.06 at $|V_{bias}|$ = 130 V and 187 V respectively, which is higher than the 0.86 ± 0.05 obtained at $|V_{bias}|$ = 0 V (Table 1). This result implies that the areal density of N atoms deposited per cycle increases in par with the areal density of Hf atoms when $|V_{bias}|$ increases.

In addition to the changes in the Hf^{3+} fraction, the variations in microstructure with $|V_{bias}|$ might also contribute to the ρ_e as

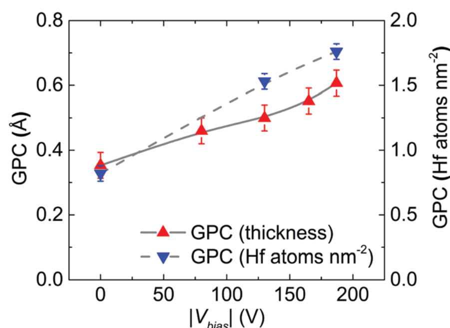

Fig. 4 Growth per cycle (GPC) in terms of thickness and number of Hf atoms deposited per nm^2 as determined by SE and RBS as a function of the absolute value of V_{bias}. Lines serve as a guide to the eye.

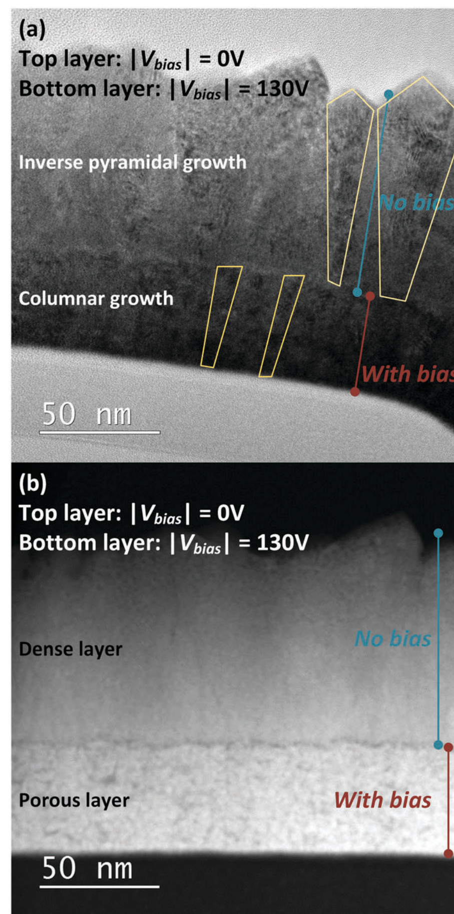

Fig. 5 (a) Bright-field transmission electron microscopy image (BF-TEM) and (b) high-angle annular dark-field scanning transmission electron microscopy (HAADF-STEM) image of the HfN_x film grown in two steps with different substrate potentials: bottom layer at $|V_{bias}|$ = 130 V and top layer at $|V_{bias}|$ = 0 V.

described by Ponomarev *et al.*[40] The microstructure of the HfN_x films was studied by evaluating the in-grain film porosity, in-grain film crystallinity, lateral grain size and residual film stress as a function of $|V_{bias}|$ (for films with a similar thickness of ∼75 nm).

First, the microstructure of the HfO_yN_x and HfN_x films grown at $|V_{bias}|$ = 0 V and $|V_{bias}|$ = 130 V respectively are compared and the grain development was scrutinized. To serve our purposes, the HfN_x ALD was carried out under two conditions in a single run (without breaking the vacuum): a ∼45 nm bottom layer grown at $|V_{bias}|$ = 130 V and a ∼85 nm top layer was grown at $|V_{bias}|$ = 0 V. The bright-field TEM (BF-TEM) image of the stack of HfN_x films is presented in Fig. 5a. The grain growth of HfN_x film prepared at $|V_{bias}|$ = 0 V was found to be inverse pyramidal whereas a columnar growth of the HfN_x film was detected at $|V_{bias}|$ = 130 V. Furthermore, the contrast variations within the crystals of the HfN_x film grown at $|V_{bias}|$ = 0 V indicate the presence of many small defects such as dislocations and/or low-angle grain boundaries. In Fig. 5b, the high-angle annular dark-field STEM (HAADF-STEM) image for the HfN_v film stack is presented elucidating that the HfN_x film grown at

 This journal is © The Royal Society of Chemistry 2018

Published on 12 March 2018. Downloaded by Eindhoven University of Technology on 28/03/2018 21:38:44.

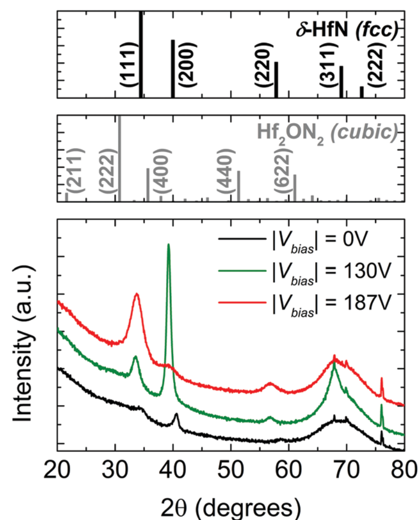

Fig. 6 X-ray diffractograms (Gonio (θ–2θ) scans) for ~75 nm thick HfN_x films for various values of $|V_{bias}|$ referenced with powder fcc δ-HfN and cubic Hf_2ON_2 XRD patterns.

$|V_{bias}|$ = 130 V is rich in nanopores whereas the HfN_x film prepared at $|V_{bias}|$ = 0 V is relatively more dense.

The crystallinity of the HfN_x films was examined using XRD (θ–2θ mode) (Fig. 6). The HfN_x films grown at $|V_{bias}|$ = 0 V are polycrystalline with a mixture of two phases: δ-HfN and cubic Hf_2ON_2, as evident from previously reported grazing incidence XRD patterns.[22,36] The θ–2θ scan of this sample in Fig. 6 shows broad peaks, which can be explained by the defect-rich nature of the grains, in-line with the TEM study. Based on the chemical composition analysis, GIXRD patterns (Fig. S7, ESI†) and θ–2θ scans, we suggest a predominant growth of the δ-HfN phase at a $|V_{bias}|$ value of 130 V and higher, whereas the Hf_2ON_2 phase is below the detection limit. The HfN_x films grown at $|V_{bias}|$ = 130 V gave a strong HfN(200) reflection implying a preferred orientation, in-line with the columnar grain growth. Furthermore, the increase in HfN(111) and HfN(200) peak intensity suggests that the crystalline quality of XRD coherent domains increased upon increasing the $|V_{bias}|$ from 0 V to 130 V, despite the introduction of voids in the film. In contrast to the HfN_x films grown at $|V_{bias}|$ = 130 V, HfN(111) is the preferred orientation at $|V_{bias}|$ = 187 V. The development of a preferred orientation during film growth can be introduced by several factors, such as the minimization of strain or surface energy.[47] This was demonstrated by Pelleg *et al.* for TiN_x films grown by PVD.[48] It was reported that the growth of TiN(200) is favoured in order to minimize the surface energy whereas TiN(111) is the preferred growth direction to minimize the strain energy.[48,49] Alternatively, the texture could already be different in the nucleation phase of the films. Interestingly, the crystallographic texture appeared to be similar for ~15 nm thick HfN_x films grown at $|V_{bias}|$ = 130 V and $|V_{bias}|$ = 187 V, as evident from the HAADF-STEM and SAED studies (see the discussion underneath in the ESI†, Fig. S8).

Subsequently, the lateral grain size of the HfN_x films was investigated for the relevant layer thickness of 75 nm by means of SEM. The HfN_x films grown with a grounded electrode ($|V_{bias}|$ = 0 V) displayed a lateral grain size of 25 ± 3 nm (Fig. 7a and Table 2). Interestingly, the 75 nm thick HfN_x layer grown at $|V_{bias}|$ value of 130 V exhibits a similar grain size of 26 ± 2 nm (Fig. 7b).

Summarizing the first part, we can conclude that the HfN_x films grown at $|V_{bias}|$ of 130 V are considerably more porous than the HfO_yN_x films grown with the grounded electrode even though the lateral grain sizes are similar for both layers. Therefore, the decrease in the ρ_e and grain boundary scattering upon increasing the $|V_{bias}|$ from 0 V to 130 V appears to be primarily a result of modification in the chemical composition. The latter stems from a decrease in O content and the associated improvement in the Hf^{3+} fraction.

Having established that the decrease in ρ_e up to $|V_{bias}|$ = 130 V is primarily driven by the modification in chemical composition, the microstructure of the HfN_x films grown at $|V_{bias}|$ = 130 V and $|V_{bias}|$ = 187 V with the same chemical composition was subsequently compared. An increment in the $|V_{bias}|$ from 130 V to 187 V led to a major decrease in the lateral grain size from 26 ± 2 nm to 18 ± 3 nm respectively (Fig. 7c), as revealed from SEM analyses.

Complementary to the lateral grain size obtained from SEM analysis, the vertical crystallite sizes for the same films were deduced for the HfN(200) and HfN(111) reflections of the XRD patterns. The difference between the grain size from SEM and the crystallite size can have two reasons; firstly, SEM yields the lateral grain size as evident on the top surface, while XRD probes the vertical grain size. Secondly, a grain may contain many defects and small angle grain boundaries. The peaks

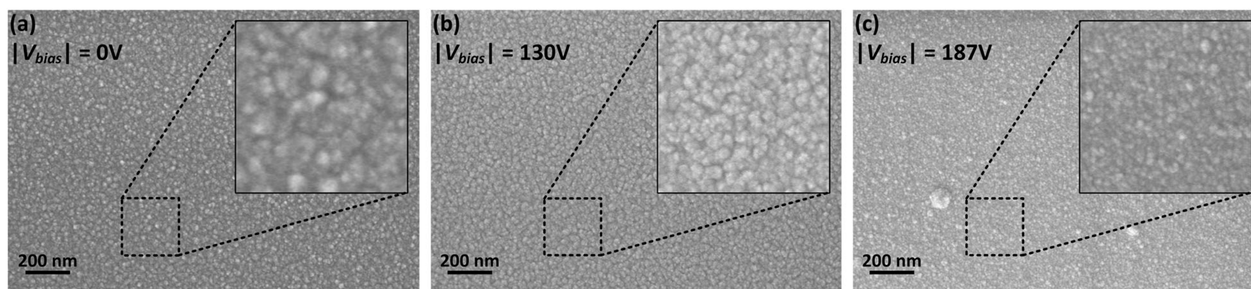

Fig. 7 Scanning electron micrographs displaying top-view for HfN_x films (thickness ~75 nm) prepared at (a) $|V_{bias}|$ = 0 V (b) $|V_{bias}|$ = 130 V and (c) $|V_{bias}|$ = 187 V. Insets depicts a magnified view of the surface morphology used to obtain lateral grain sizes.

Published on 12 March 2018. Downloaded by Eindhoven University of Technology on 28/03/2018 21:38:44.

Table 2 Grain size and residual stress values for HfN_x films (thickness ~75 nm) prepared under various values of $|V_{bias}|$. The lateral grain sizes are determined *via* SEM. The crystallite size is obtained from XRD using Scherrer's equation for the corresponding diffracting planes ($h\,k\,l$). Typical errors associated with the measured quantities are indicated. The film stress has been determined by wafer curvature measurements

	SEM	XRD		
$\|V_{bias}\|$ (V)	Grain size (nm)	Peak ($h\,k\,l$)	Crystallite size (nm)	Residual compressive stress σ_{11} (GPa)
0	25 ± 3	200	—	—
		111	—	
130	26 ± 2	200	10.6 ± 0.1	2.00 ± 0.05
		111	6.2 ± 0.2	
187	18 ± 3	200	—	0.34 ± 0.03
		111	3.6 ± 0.1	

widths in XRD scans represent the lengths of the coherent diffraction domains in a crystal. Therefore, the crystallite size might be smaller or equal to the grain size. The data in Table 2 indicates the formation of relatively larger crystallites at $|V_{bias}|$ = 130 V. On the other hand, an increment in the $|V_{bias}|$ to 187 V gives an apparent broad peak for the HfN(111) reflection yielding a relatively smaller crystallite size. A comparison with the BF-TEM image in Fig. 5a shows that the crystallite size as determined from XRD is significantly smaller than the column height, which can be understood from the limited XRD coherence due to the porous and defect-rich nature of the layer. Furthermore, it should be also noted that the peak broadening may also result from the presence of residual stress in the layers.[37]

The residual stress for the HfN_x films grown at varied $|V_{bias}|$ was determined by means of wafer curvature measurements and is presented in Table 2.[38] The data displays a much higher compressive residual stress for the HfN_x films deposited at $|V_{bias}|$ = 130 V as compared to that at $|V_{bias}|$ = 187 V. Liao *et al.* demonstrated that the resistivity of HfN_x films, grown by PVD, can significantly depend on the residual stresses, *i.e.* high residual stress can lead to a lower ρ_e.[38] Therefore the lower ρ_e at $|V_{bias}|$ = 130 V may also partly arise from the high residual stress in the layer. Additionally, it can be concluded that the broadening of peaks in XRD at $|V_{bias}|$ = 187 V is primarily due to decrease in the vertical crystallite size. In addition, a discrete SAED pattern is obtained for the ~15 nm thick HfN_x film prepared at $|V_{bias}|$ = 130 V whereas the HfN_x film grown at $|V_{bias}|$ = 187 V exhibits a continuous pattern. This suggests that the lateral crystallite size is also smaller for the HfN_x film grown at $|V_{bias}|$ = 187 V (see ESI,† Fig. S8).

Based on the microstructural characterization, it can be concluded that an increase in ρ_e and grain boundary scattering at $|V_{bias}|$ above 130 V is primarily a consequence of a major decrease in lateral grain size as well as in-the grain crystalline quality in both vertical and lateral directions, since the chemical composition of the HfN_x films grown above $|V_{bias}|$ = 130 V is similar.

Having established that the ρ_e is related to the chemical composition of the HfN_x films in the range of $|V_{bias}|$ up to 130 V, the chemical composition of the HfN_x films was investigated on

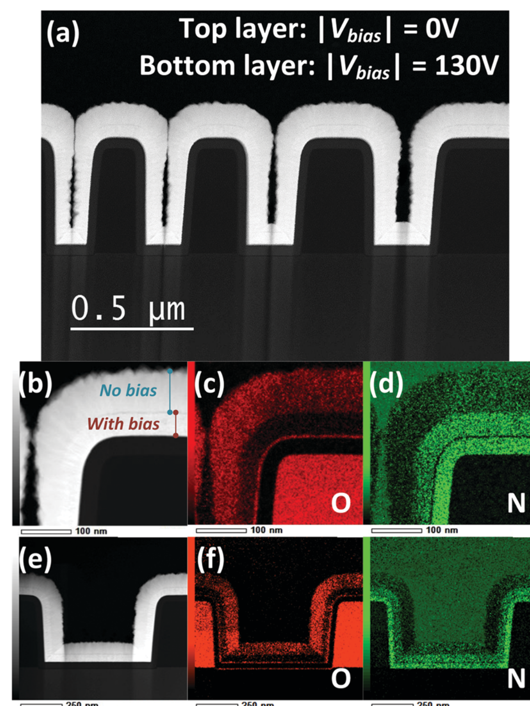

Fig. 8 (a) High-angle annular dark-field scanning transmission electron microscopy (HAADF-STEM) image of the HfN_x film grown in two steps with different substrate potentials: bottom layer at $|V_{bias}|$ = 130 V and top layer with grounded electrode ($|V_{bias}|$ = 0 V) (b and e) higher magnification HAADF-STEM images containing both planar and vertical topography and EDX elemental mappings of (c and f) O and (d and g) N. The trench aspect ratio for (b–d) was 2:1 and 1:1 for (e–g).

3D topographies which is relevant for advanced nanoscale device architectures. The HAADF-STEM image of HfN_x films grown on 3D trench nanostructures is presented in Fig. 8. A stack of HfN_x films was prepared in a single run with an ~45 nm bottom layer grown at $|V_{bias}|$ = 130 V and a ~85 nm top layer grown at $|V_{bias}|$ = 0 V, as aforementioned. Magnified HAADF-STEM images for a trench with an aspect ratio of 2:1 and 1:1 are presented in Fig. 8b and e. The difference in the chemical compositions of the two HfN_x films grown at different values of $|V_{bias}|$ is clearly evident from the EDX elemental mapping (Fig. 8c, f and d, g), in agreement with Table 1. On planar surfaces, the HfN_x layer grown at $|V_{bias}|$ = 130 V was found to contain no O, whereas O was present in abundance in the HfN_x layer grown at $|V_{bias}|$ = 0 V (Fig. 8c and f), in-line with the RBS findings. Moreover, the HfN_x layer grown at $|V_{bias}|$ = 130 V was found to be relatively richer in N content as compared to the film grown at $|V_{bias}|$ = 0 V (Fig. 8d and g), also in-line with the RBS results.

Considering the sidewalls of the trenches, a higher O content and relatively lower N content was noted in comparison with planar surfaces at $|V_{bias}|$ = 0 V. This relates to the fact that the sidewalls are exposed to a much lower ion flux as compared to the planar surfaces due to directionality of the ions. Strikingly, the sidewalls of HfN_x film grown at $|V_{bias}|$ = 130 V appears to contain less oxygen than the planar surfaces of HfN_x film grown at $|V_{bias}|$ = 0 V. Similarly, nitrogen appears to be higher in

This journal is © The Royal Society of Chemistry 2018

Published on 12 March 2018. Downloaded by Eindhoven University of Technology on 28/03/2018 21:38:44.

concentration on the sidewalls of the HfN_x film grown at $|V_{bias}|$ = 130 V with respect to the planar surfaces of HfN_x film grown at $|V_{bias}|$ = 0 V. This may be a consequence of ion bombardment present also on the sidewalls due to ions colliding in the plasma sheath which allows the ions to reach the sidewalls, but with a lower flux and energy. Indeed, the plasma sheath appears not to be fully collisionless as will be addressed in follow-up work on the basis of actual ion energy measurements.

Conclusions

A plasma-assisted HfN_x ALD process has been reported employing $CpHf(NMe_2)_3$ as the Hf precursor and H_2 plasma as the reducing co-reactant. The application of an external rf substrate bias during the H_2 plasma half cycle has been addressed in order to study the effects of an increase in the energy of ions impinging on the surface during film growth. It has been shown that the electrical resistivity of the HfN_x films decreased from 9.0×10^{-1} Ω cm to 3.3×10^{-3} Ω cm upon increasing the $|V_{bias}|$ from 0 V to 130 V respectively. A further increase in $|V_{bias}|$ to 187 V led to an increase in film resistivity to 1.0×10^{-2} Ω cm. Furthermore, we showed that the variations in electrical resistivity with $|V_{bias}|$ correlated with the grain boundary scattering in the films, which significantly decreased upon increasing $|V_{bias}|$ up to 130 V. The decrease in electrical resistivity and scattering is the result of a major improvement in chemical composition. The latter stems from a major decrease in the O content from 20.1 at% at no bias to ≤ 2 at% at a $|V_{bias}|$ of 130 V or higher and the associated increase in the Hf^{3+} oxidation state fraction from 0.65 to 0.82 respectively. Microstructural analyses revealed that the HfN_x films prepared at $|V_{bias}|$ = 130 V are more porous than films grown with a grounded electrode whereas the lateral grain sizes are similar. On the other hand, the grain boundary scattering increased at $|V_{bias}|$ above 130 V primarily due to a major decrease in grain size as well as in-grain crystalline quality. Furthermore, the HfN_x was also deposited at $|V_{bias}|$ = 130 V on 3D trench nanostructures. A low O content in the HfN_x film was obtained on the planar as well as vertical regions of the trench structures, attributed to collisions in the plasma sheath leading to some ion bombardment on the sidewalls as well. In conclusion, we demonstrate that the energy of bombarding ions during plasma-assisted ALD play a vital role in improving the chemical composition, microstructure and electrical properties of the HfN_x films and may be extended to related nitrides.

Conflicts of interest

All authors have given approval to the final version of the manuscript. There are no conflicts to declare.

Acknowledgements

The authors thank Dr Mike Cooke, Dr Vincent Vandalon, Dr Janne-Petteri Niemelä and Dr Harm Knoops for fruitful discussions. LAM research is acknowledged for preparing and providing the coupons with trench nanostructures and B. Barcones is acknowledged for the FIB preparation of the TEM samples, and Cristian van Helvoirt and Jeroen van Gerwen for the skillful technical assistance. The authors would also like to thank Vivek Beladiya (University of Jena) for the meaningful stress measurements. Solliance and the Dutch province of Noord-Brabant are acknowledged for funding the TEM facility. This work was supported financially by Technologiestichting STW through the project LIMIET. Air Liquide is kindly acknowledged for providing the Hf precursor.

References

1 Y. Liu, T. Nabatame, N. Nguyen, T. Matsukawa, K. Endo, S. O'Uchi, J. Tsukada, H. Yamauchi, Y. Ishikawa, W. Mizubayashi, Y. Morita, S. Migita, H. Ota, T. Chikyow and M. Masahara, *Jpn. J. Appl. Phys.*, 2015, 54.
2 H. O. Pierson, *Handbook of Refractory Carbides and Nitrides: Properties, Characteristics, Processing and Apps*, Elsevier Science, 1996.
3 C. K. Hu and J. M. E. Harper, *Mater. Chem. Phys.*, 1998, **52**, 5–16.
4 W. Jeong, Y. Ko, S. Bang, S. Lee and H. Jeon, *J. Korean Phys. Soc.*, 2010, **56**, 905–910.
5 H. Kim, C. Cabral, C. Lavoie and S. M. Rossnagel, *J. Vac. Sci. Technol., B: Microelectron. Nanometer Struct. – Process., Meas., Phenom.*, 2002, **20**, 1321–1326.
6 H. Y. Yu, J. F. Kang, C. Ren, J. D. Chen, Y. T. Hou, C. Shen, M. F. Li, D. S. H. Chan, K. L. Bera, C. H. Tung and D. L. Kwong, *IEEE Electron Device Lett.*, 2004, **25**, 70–72.
7 A. D. Franklin, S. O. Koswatta, D. B. Farmer, J. T. Smith, L. Gignac, C. M. Breslin, S.-J. Han, G. S. Tulevski, H. Miyazoe, W. Haensch and J. Tersoff, *Nano Lett.*, 2013, **13**, 2490–2495.
8 H. Y. Yu, M. F. Li and D. L. Kwong, *IEEE Trans. Electron Devices*, 2004, **51**, 609–615.
9 C. Hu, Z. Gu, J. Wang, K. Zhang, X. Zhang, M. Li, S. Zhang, X. Fan and W. Zheng, *J. Phys. Chem. C*, 2014, **118**, 20511–20520.
10 M. Strømme, R. Karmhag and C. G. Ribbing, *Opt. Mater.*, 1995, **4**, 629–639.
11 J. Malmström, S. Schleussner and L. Stolt, *Appl. Phys. Lett.*, 2004, **85**, 2634–2636.
12 K. E. Andersson, M. Veszelei and A. Roos, *Sol. Energy Mater. Sol. Cells*, 1994, **32**, 199–212.
13 B. Karlsson and C. G. Ribbing, *Proc. SPIE*, 1982, **0324**, 52–57.
14 M. Xu, S. Wang, G. Yin, J. Li, Y. Zheng, L. Chen and Y. Jia, *Appl. Phys. Lett.*, 2006, 89.
15 J. S. Becker, E. Kim and R. G. Gordon, *Chem. Mater.*, 2004, **16**, 3497–3501.
16 I. L. Farrell, R. J. Reeves, A. R. H. Preston, B. M. Ludbrook, J. E. Downes, B. J. Ruck and S. M. Durbin, *Appl. Phys. Lett.*, 2010, 96.
17 B. O. Johansson, U. Helmersson, M. K. Hibbs and J. E. Sundgren, *J. Appl. Phys.*, 1985, **58**, 3104–3111.
18 H. S. Seo, T. Y. Lee, J. G. Wen, I. Petrov, J. E. Greene and D. Gall, *J. Appl. Phys.*, 2004, **96**, 878–884.

Published on 12 March 2018. Downloaded by Eindhoven University of Technology on 28/03/2018 21:38:44.

19 Y. Kim, A. Baunemann, H. Parala, A. Devi and R. A. Fischer, *Chem. Vap. Deposition*, 2005, **11**, 294–297.
20 S. Consiglio, W. Zeng, N. Berliner and E. T. Eisenbraun, *J. Electrochem. Soc.*, 2008, **155**, H196–H201.
21 E. J. Kim and D. H. Kim, *Electrochem. Solid-State Lett.*, 2006, **9**, C123–C125.
22 S. Karwal, B. L. Williams, J. P. Niemelä, M. A. Verheijen, W. M. M. Kessels and M. Creatore, *J. Vac. Sci. Technol., A*, 2017, 35.
23 J. W. Elam, J. A. Libera, T. H. Huynh, H. Feng and M. J. Pellin, *J. Phys. Chem. C*, 2010, **114**, 17286–17292.
24 S. Haukka, E.-L. Lakomaa, O. Julha, J. Vilhunen and S. Hornytzkyj, *Langmuir*, 1993, **9**, 3497–3506.
25 E. L. Lakomaa, A. Root and T. Suntola, *Appl. Surf. Sci.*, 1996, **107**, 107–115.
26 J. Keranen, C. Guimon, E. Iiskola, A. Auroux and L. Niinisto, *J. Phys. Chem. B*, 2003, **107**, 10773–10784.
27 A. Anders, *Thin Solid Films*, 2010, **518**, 4087–4090.
28 L. Martinu, O. Zabeida and J. E. Klemberg-Sapieha, *Handbook of Deposition Technologies for Films and Coatings*, William Andrew Publishing, *Boston*, 3rd edn, 2010, pp. 392–465, DOI: 10.1016/B978-0-8155-2031-3.00009-0.
29 S. G. Walton and J. E. Greene, *Handbook of Deposition Technologies for Films and Coatings*, William Andrew Publishing, *Boston*, 3rd edn, 2010, pp. 32–92, DOI: 10.1016/B978-0-8155-2031-3.00002-8.
30 H. B. Profijt, M. C. M. Van De Sanden and W. M. M. Kessels, *J. Vac. Sci. Technol., A*, 2013, 31.
31 H. C. M. Knoops, E. M. J. Braeken, K. De Peuter, S. E. Potts, S. Haukka, V. Pore and W. M. M. Kessels, *ACS Appl. Mater. Interfaces*, 2015, **7**, 19857–19862.
32 H. C. M. Knoops, K. De Peuter and W. M. M. Kessels, *Appl. Phys. Lett.*, 2015, 107.
33 H. B. Profijt, S. E. Potts, M. C. M. Van De Sanden and W. M. M. Kessels, *J. Vac. Sci. Technol., A*, 2011, **29**, 050801.
34 H. C. M. Knoops, B. W. H. van de Loo, S. Smit, M. V. Ponomarev, J.-W. Weber, K. Sharma, W. M. M. Kessels and M. Creatore, *J. Vac. Sci. Technol., A*, 2015, **33**, 021509.
35 I. I. Timofeeva and L. K. Shvedova, *Izv. Akad. Nauk SSSR, Neorg. Mater.*, 1972, **8**, 1169–1170.
36 W. Wang, T. Nabatame and Y. Shimogaki, *Microelectron. Eng.*, 2008, **85**, 320–326.
37 H. P. Klug and L. E. Alexander, *X-Ray Diffraction Procedures: For Polycrystalline and Amorphous Materials*, Wiley, 1974.
38 M. Y. Liao, Y. Gotoh, H. Tsuji and J. Ishikawa, *J. Vac. Sci. Technol., A*, 2004, **22**, 214–220.
39 R. A. Ovanesyan, D. M. Hausmann and S. Agarwal, *ACS Appl. Mater. Interfaces*, 2015, **7**, 10806–10813.
40 M. V. Ponomarev, M. A. Verheijen, W. Keuning, M. C. M. van de Sanden and M. Creatore, *J. Appl. Phys.*, 2012, **112**, 043708.
41 P. D. Kirsch, C. S. Kang, J. Lozano, J. C. Lee and J. G. Ekerdt, *J. Appl. Phys.*, 2002, **91**, 4353–4363.
42 A. N. Kornilov, I. M. Ushakova, E. J. Huber Jr and C. E. Holley Jr, *J. Chem. Thermodyn.*, 1975, **7**, 21–26.
43 A. D. Mah and N. L. Gellert, *J. Am. Chem. Soc.*, 1956, **78**, 3261–3263.
44 S. Shinkai and K. Sasaki, *Jpn. J. Appl. Phys., Part 1*, 1999, **38**, 2097–2102.
45 W. Wang, T. Nabatame and Y. Shimogaki, *Surf. Sci.*, 2005, **588**, 108–116.
46 J. H. Jang, T. J. Park, J. H. Kim, K. D. Na, W. Y. Park, M. Kim and C. S. Hwang, *J. Electrochem. Soc.*, 2009, **156**, H76–H79.
47 C. V. Thompson, *Annu. Rev. Mater. Sci.*, 2000, **30**, 159–190.
48 J. Pelleg, L. Z. Zevin, S. Lungo and N. Croitoru, *Thin Solid Films*, 1991, **197**, 117–128.
49 U. C. Oh and J. H. Je, *J. Appl. Phys.*, 1993, **74**, 1692–1696.

 This journal is © The Royal Society of Chemistry 2018